Journal of Solid State Chemistry 253 (2017) 347–354

Contents lists available at ScienceDirect

Journal of Solid State Chemistry

journal homepage: www.elsevier.com/locate/jssc

Magnetic properties of the 6H perovskite $Ba_3Fe_2TeO_9$

Yawei Tang[a], Robert Paria Sena[b], Maxim Avdeev[c,d], Peter D. Battle[a,*], J.M. Cadogan[e], Joke Hadermann[b], Emily C. Hunter[a]

[a] Inorganic Chemistry Laboratory, Oxford University, South Parks Road, Oxford OX1 3QR, UK
[b] EMAT, University of Antwerp, Groenenborgerlaan 171, 2020 Antwerp, Belgium
[c] Australian Nuclear Science and Technology Organisation, Lucas Heights, NSW2234, Australia
[d] School of Chemistry, The University of Sydney, Sydney, NSW 2006, Australia
[e] School of Physical, Environmental and Mathematical Sciences, UNSW Canberra at the Australian Defence Force Academy, Canberra, BC 2610, Australia

ARTICLE INFO

Keywords:
6H perovskite
Antiferromagnetism

ABSTRACT

A polycrystalline sample of $Ba_3Fe_2TeO_9$ having the 6H perovskite structure has been prepared in a solid-state reaction and studied by a combination of electron microscopy, Mössbauer spectroscopy, magnetometry, X-ray diffraction and neutron diffraction. Partial ordering of Fe^{3+} and Te^{6+} cations occurs over the six-coordinate sites; the corner-sharing octahedra are predominantly occupied by the former and the face-sharing octahedra by a 1:1 mixture of the two. On cooling through the temperature range $18 < T/K < 295$ an increasing number of spins join an antiferromagnetic backbone running through the structure while the remainder show complex relaxation effects. At 3 K an antiferromagnetic phase and a spin glass coexist.

1. Introduction

The structure of a cubic perovskite ABO_3 can be considered to consist of pseudo-close-packed AO_3 layers stacked in a cubic-close-packed (ccp) sequence, with B cations occupying six-coordinate interstitial sites between the layers; the layers lie perpendicular to the [111] axis of the cubic unit cell. As the size of the cation A increases relative to that of the cation B, the stacking sequence of the layers changes from ccp to hexagonal-close-packed (hcp), with the layers now lying perpendicular to the [001] axis of a hexagonal unit cell. $BaMnO_3$ and $BaNiO_3$ exemplify the hcp structure [1,2]. One significant consequence of the change in stacking sequence is that the connectivity between BO_6 octahedra switches from vertex-sharing to face-sharing, thus introducing short contacts between B cations. The switch from ccp stacking to hcp stacking is not always complete. Many compounds exhibit mixed stacking sequences, with the so-called 6H structure, based on the six-layer *cchcch* sequence being particularly common. This structure contains B_2O_9 dimers, formed by face sharing BO_6 octahedra, which are linked together by single, vertex-sharing BO_6 octahedra. The six-coordinate sites in many perovskites, both pseudo-cubic and hexagonal, are occupied by more than one species of cation, leading to the use of formulae of the form $A_2BB'O_6$ and $A_3B_2B'O_9$ in cases where the distribution of cations is non-random and a particular cation species has a preference for one of the crystallographically-distinct sites. This cation ordering can have a marked effect on the physical properties of the compound.

The variation of cation radius down Group 2 of the Periodic Table is such that it is common for a strontium-containing perovskite to be pseudo-cubic and for the barium-containing analogue to have a mixed or hexagonal stacking sequence [3,4]. The two compounds are often reported together in the literature, with attention being focussed on the structural change and the resulting differences in physical properties. $Sr_3Fe_2TeO_9$ and $Ba_3Fe_2TeO_9$ constitute one such pair of compounds [5,6]. They have also been studied independently and we have recently concluded our own investigation into $Sr_3Fe_2TeO_9$ [7]. That study revealed a hitherto undetected complexity in the structural chemistry, including the occurrence of unusual 2:1 cation ordering in the pseudo-cubic structure. The earliest study [8] of $Ba_3Fe_2TeO_9$ identified a 6H structure with Fe^{3+} in the vertex sharing octahedra and a disordered distribution of Fe^{3+} and Te^{6+} in the dimers. The compound was found to show weak ferromagnetism below 220 K. Gagulin et al. [9] carried out the first neutron diffraction study of $Ba_3Fe_2TeO_9$ and concluded that it is a Seignette-magnet, the name given to multiferroic materials when they were last the focus of research interest. Augsburger et al. [6] found evidence for cation disorder in their sample, which they found to be magnetic below 711 K. In contrast, the sample prepared by Djerdj et al. [10] was described as paramagnetic above 100 K and showed a susceptibility maximum at 20 K.

There is clearly disagreement over the magnetic properties of $Ba_3Fe_2TeO_9$. We have therefore undertaken a study in which low-temperature neutron diffraction and Mössbauer spectroscopy have been used for the first time to resolve some of the controversial issues.

* Corresponding author.
E-mail address: peter.battle@chem.ox.ac.uk (P.D. Battle).

http://dx.doi.org/10.1016/j.jssc.2017.06.019
Received 20 May 2017; Received in revised form 19 June 2017; Accepted 20 June 2017
Available online 22 June 2017

We have also used high-resolution transmission electron microscopy to look more closely at the distribution of the cations occupying the dimers within the 6H structure. Our results are described below.

2. Experimental

A polycrystalline sample of $Ba_3Fe_2TeO_9$ was prepared using the standard ceramic method. $BaCO_3$, Fe_2O_3 and TeO_2 (purity > 99.95%) were weighed out in the appropriate stoichiometric ratio and ground together in an agate mortar for 30 min to give a homogeneous mixture. The mixture was then loaded into an alumina crucible and fired at 700 °C for 24 h. It was then quenched to room temperature, reground and pressed into a pellet that was fired in air at 950 °C for 24 h and subsequently annealed at 1200 °C for 48 h after further grinding. Finally, the furnace was allowed to cool to 800 °C and then the sample was quenched to room temperature.

The brown reaction product was initially characterised by X-ray powder diffraction (XRPD) using Cu $K\alpha_1$ radiation. The data, collected at room temperature on a Panalytical X'Pert diffractometer, were analysed using the Rietveld method as implemented in the GSAS [11] program package. Neutron diffraction data were subsequently collected on the diffractometer Echidna at the Bragg Institute, ANSTO, Australia. The angular region $10 < 2\theta/° < 162.5$ was scanned in steps of 0.05° at temperatures of 300, 250, 200, 150, 100, 50 and 3 K using neutron wavelengths of 1.6215(5) or 2.4395(5) Å as appropriate. Data analysis was again performed using the Rietveld method [12]. The peak shape was modelled using the function devised by van Laar and Yelon [13] and the background was fitted using a twelve-term Chebyschev polynomial.

The magnetic susceptibility of $Ba_3Fe_2TeO_9$ was measured over the temperature range $2 < T/K < 300$ using a Quantum Design MPMS 5000 SQUID magnetometer. Data were collected on warming in fields of 100 and 1000 Oe after cooling the sample both in the absence of an applied field (zero-field cooled, ZFC) and in the measuring field (field cooled, FC). The isothermal sample magnetisation was measured as a function of field over the range $-50 < H/kOe < 50$ at 5 K after cooling in a field of 50 kOe.

Samples for transmission electron microscopy were prepared by crushing the powder of $Ba_3Fe_2TeO_9$, dispersing it in ethanol and depositing a few drops of this suspension on a holey carbon grid. High angle annular dark field and annular bright field scanning transmission electron microscopy (HAADF-STEM and ABF-STEM) images were recorded with an aberration-corrected FEI Titan G3 microscope operating at 300 kV. Calculated images were produced using QSTEM 2.2 [14].

^{57}Fe Mössbauer spectra of finely ground $Ba_3Fe_2TeO_9$ were acquired at 295 K, 200 K, 100 K and 13 K using a standard spectrometer operating in transmission mode with a ^{57}CoRh source. All spectra, except that at 295 K, were obtained using a vibration-isolated closed-cycle refrigerator. The spectrometer's velocity scale was calibrated using a 6 μm thick α-Fe foil at 295 K and all isomer shifts (δ) quoted in this paper are relative to the centre of the α-Fe calibration spectrum. All Mössbauer spectra were fitted using the NORMOS software [15].

3. Results

The XRPD pattern of the reaction product suggested that the synthesis had produced a phase-pure 6H hexagonal perovskite. Influenced by the earlier work of Augsburger et al. [6], we first indexed and analysed the pattern in the hexagonal space group $P6_3/mmc$. Reasonably good agreement between the observed and calculated diffraction patterns was achieved with $R_{wpr} = 5.40\%$, $\chi^2 = 1.85$, see Fig. 1. The unit-cell parameters refined to values of $a = 5.76882(2)$ Å, $c = 14.19859(6)$ Å. This structural model, see Fig. 2(a), contains two independent A sites, 2*b* (0, 0, ¼) and 4*f* (⅓, ⅔, *z*) which accommodate Ba^{2+} cations and two B sites, 2*a* (0, 0, 0) and 4*f* (⅓, ⅔, *z*), for Fe^{3+} and

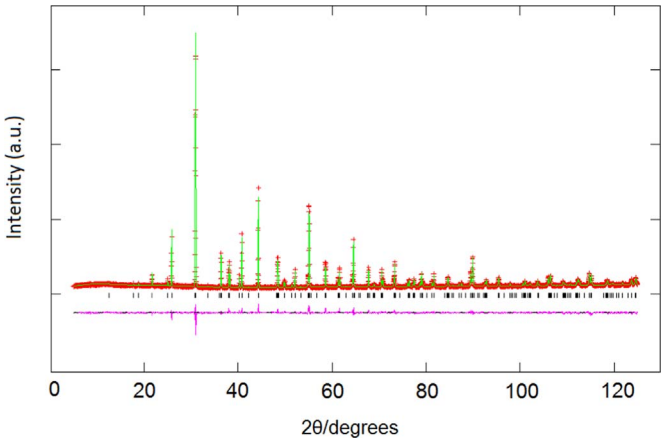

Fig. 1. Observed (red), calculated (green) XRPD patterns of $Ba_3Fe_2TeO_9$ at room temperature. A difference curve (purple) is shown and reflection positions are marked. (For interpretation of the references to color in this figure legend, the reader is referred to the web version of this article.)

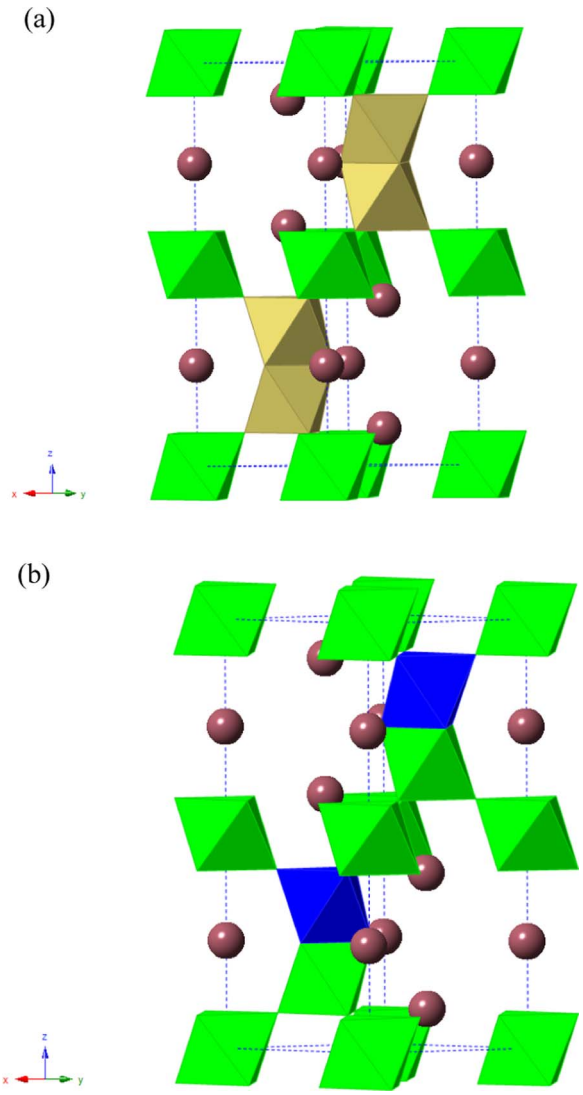

Fig. 2. (a) $P6_3/mmc$ and (b) $P6_3mc$ structure of $Ba_3Fe_2TeO_9$. Green octahedra are occupied largely by Fe, khaki octahedra are occupied by a disordered arrangement of Fe and Te and blue octahedra are occupied largely by Te. Mauve circles represent Ba atoms. (For interpretation of the references to color in this figure legend, the reader is referred to the web version of this article.)

Te^{6+} cations. The 2*a* B sites lie at the centre of the vertex-sharing octahedra and the 4*f* B sites lie within the M_2O_9 dimers. The shared face of the dimers is formed by three O1 ions on 6*h* (*x*, 2*x*, ¼) sites and the O2 ions on 12*k* (*x*, 2*x*, *z*) sites connect the dimers to the vertex-sharing octahedra. Refinements of the distribution of Fe and Te over the crystallographically-distinct B sites showed that the 2*a* (0,0,0) sites are largely occupied by Fe and that Fe/Te are randomly distributed over the 4*f* (1/3, 2/3, z) sites. The refined cation distribution can be represented by the formula $Ba_3(Fe_{0.92}Te_{0.08})_{2a}(Fe_{0.53}Te_{0.47})_{4f}O_9$.

Structure refinements were also carried out in the non-centrosymmetric space group $P6_3mc$, in which the two cation sites within the M_2O_9 dimers are inequivalent. The reflection conditions of this group are the same as those of $P6_3/mmc$ and the agreement factors resulting from the analyses in the former, R_{wpr} = 5.53%, χ^2 = 1.94, were only slightly worse than those achieved in centrosymmetric $P6_3/mmc$. The essential difference between the two models is that in $P6_3/mmc$ the sites in the dimer are occupied in a disordered manner whereas in $P6_3mc$ the cations adopt an ordered, or partially ordered, distribution over these sites, see Fig. 2. The correct space group was determined by considering the [100] HAADF-STEM image recorded in the electron microscope. The brightness of the dots in this type of image increases with the average atomic number along the column of atoms that the dot represents. The calculated images for both models are compared to the experimental image in Fig. 3(a). In this figure the brightest dots are the projected Ba columns, the weaker ones the columns containing Fe and Te, see Fig. 3(b). The difference between the two calculated images lies in the columns of B cations occupying the sites within the dimers. One such pair, along with a neighbouring Ba column, is encircled on the experimental image, on each of the calculated images and in Fig. 3(b). In $P6_3/mmc$ these two sites are equivalent because of the mirror plane perpendicular to the c-axis, whereas in $P6_3mc$ they are independent positions (2*b* of $P6_3mc$). Analysis of the X-ray diffraction data in $P6_3mc$ results in these 2*b* positions taking on different Fe:Te ratios which can be seen in the calculated image as a systematic brightness difference between the two columns for both thin and relatively thick areas of the crystal. In $P6_3/mmc$, the two columns have the same brightness in the calculated images for thicker areas and only in very thin areas (few atoms per projected column) will the random occupation of the 4*f* site by either Te or Fe give a difference in brightness between the two columns. In the experimental image shown in Fig. 3(a) the columns in the thick regions away from the edge of the crystallite have equal brightness and thus match the image calculated for $P6_3/mmc$. The difference in the Fe:Te ratio on the crystallographically distinct 2*a* and 4*f* B positions of $P6_3/mmc$ is also clear in the HAADF-STEM images. The white dots representing columns of Fe and Te in Fig. 3(a) come in groups of three and the middle one is always the darkest. One such group is identified by the rectangle drawn on both the experimental image and the model in Fig. 3. It can be seen that the outer two dots correspond to the 4*f* columns and the experimentally darker middle dot corresponds to the 2*a* column. The 2*a* column is thus Fe-rich, in agreement with the cation distribution determined by X-ray diffraction.

In the light of the electron-microscopy results, the neutron diffraction data collected at 300 K were analysed in the space group $P6_3/mmc$. The refined atomic parameters and the agreement factors are listed in Table 1 and the most significant bond lengths and bond angles are presented in Table 2. The cation distribution over the sites within the dimers refined to be $Ba_3(Fe_{0.93}Te_{0.07})_{2a}(Fe_{0.53}Te_{0.47})_{4f}O_9$, which is in good agreement with that determined by XRPD. The resulting agreement between the observed and calculated profiles can be seen in Fig. 4; this fit was obtained without assigning ordered magnetic moments to any of the cations.

The temperature dependence of the molar magnetic susceptibility of our sample of $Ba_3Fe_2TeO_9$ measured in 100 G is shown in Fig. 5(a). The ZFC and FC susceptibilities are essentially equal above 250 K and

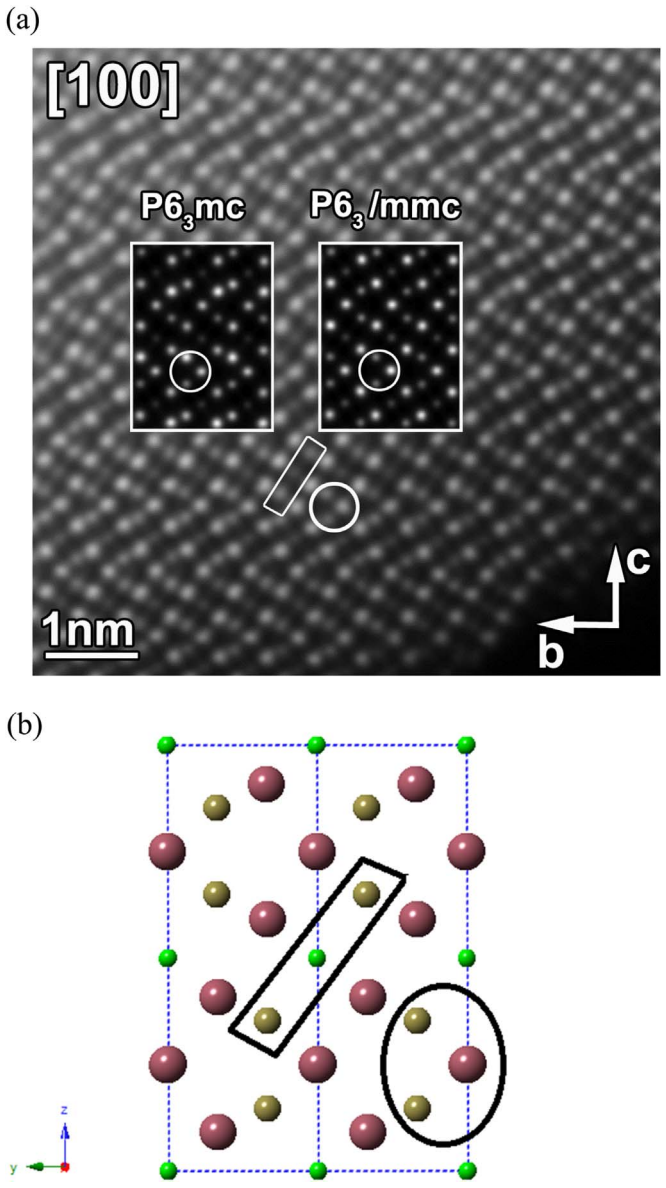

Fig. 3. (a) Aberration-corrected high angle annular dark field scanning transmission electron microscopy (HAADF-STEM) image of $Ba_3Fe_2TeO_9$ along the [100] zone axis and calculated HAADF-STEM images (b)The cation arrangement within the structure in space group $P6_3/mmc$, viewed along [100]. Green, khaki and mauve circles represent Fe (2*a* site), disordered Te/Fe (4*f* site) and Ba, respectively. (For interpretation of the references to color in this figure legend, the reader is referred to the web version of this article.)

Table 1
Atomic parameters of $Ba_3Fe_2TeO_9$, refined from neutron diffraction data collected at 300 K.

Atom	Site	*x*	*y*	*z*	U_{iso}/Å^2	Fractional occupancy
Ba1	2b	0	0	0.25	0.0050(5)	1.0
Ba2	4f	⅓	⅔	0.0919(1)	0.0062(4)	1.0
Fe1	2a	0	0	0	0.0065(5)	0.933(16)
Fe2	4f	⅓	⅔	0.85236(9)	0.0088(4)	0.529(8)
Te1	2a	0	0	0	0.0065(5)	0.067(16)
Te2	4f	⅓	⅔	0.85236(9)	0.0088(4)	0.471(8)
O1	6h	0.5153(2)	0.0306(3)	0.25	0.0111(4)	1.0
O2	12k	0.8314(2)	0.6628(3)	0.08198(7)	0.0093(2)	1.0

Space group $P6_3/mmc$, a = 5.76622(6) Å, c = 14.1966(2) Å.
R_{wp} = 4.62%, R_p = 3.69%, χ^2 = 3.754.

Table 2
Selected interatomic distances (Å) and bond angles (°) in $Ba_3Fe_2TeO_9$ at 300 K and 3 K.

	300 K	3 K
Ba1 – O1	2.88715(9) × 6	2.88095(7) × 6
Ba1 – O2	2.920(1) × 6	2.9126(9) × 6
Ba2 – O1	2.888(2) × 3	2.876(1) × 3
Ba2 – O2	2.8866(1) × 6	2.88071(7) × 6
	2.967(2) × 3	2.966(1) × 3
Fe1/Te1 – O2	2.047(1) × 6	2.046(1) × 6
Fe2/Te2 – O1	2.097(2) × 3	2.093(1) × 3
Fe2/Te2 – O2	1.891(2) × 3	1.885(1) × 3
O1 – Fe2/Te2 – O1	77.27(6)	77.49(5)
O2 – Fe1/Te1 – O2	89.13(5)	89.19(4)
	90.87(5)	90.81(4)
O2 – Fe2/Te2 – O2	97.78(6)	97.74(4)
O1 – Fe2/Te2 – O2	165.67(7)	165.85(6)
	91.61(3)	91.54(3)

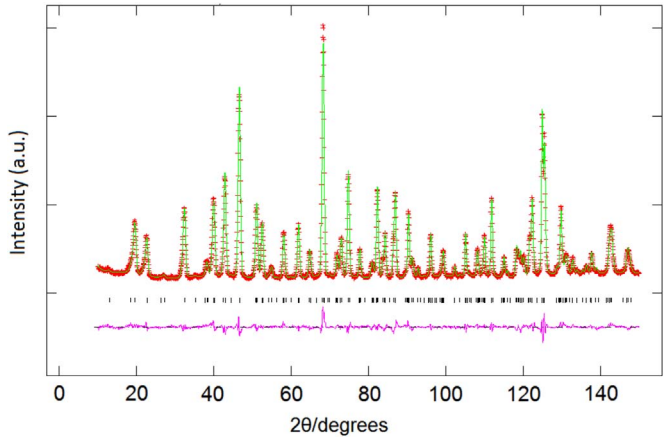

Fig. 4. Observed (red), calculated (green) neutron diffraction patterns of $Ba_3Fe_2TeO_9$ at room temperature. A difference curve (purple) is shown and reflection positions are marked. (For interpretation of the references to color in this figure legend, the reader is referred to the web version of this article.)

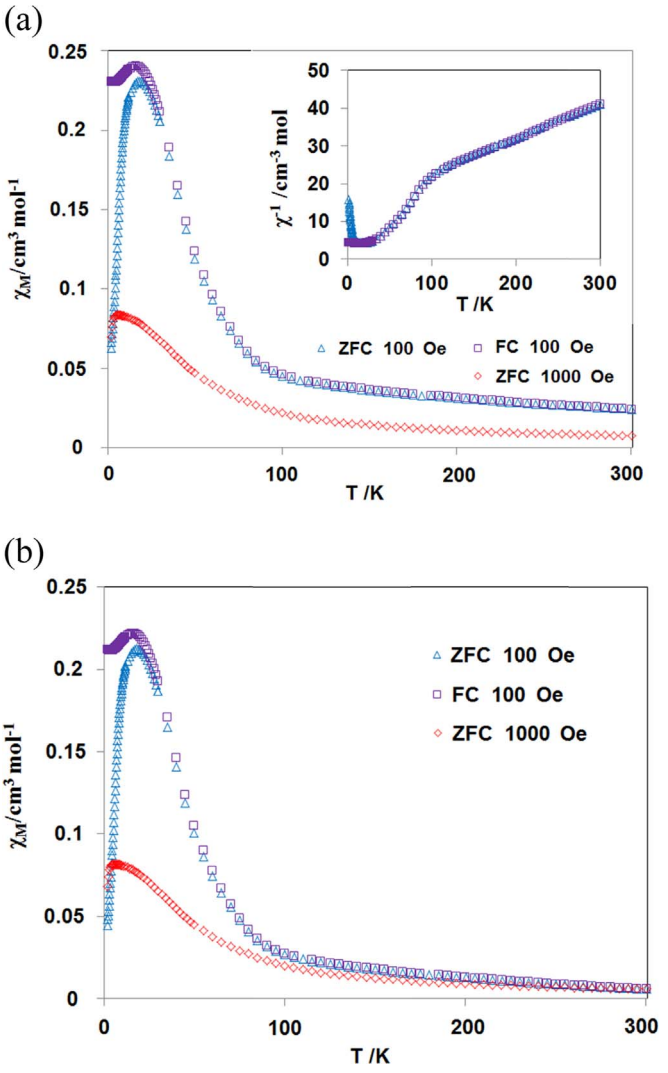

Fig. 5. Temperature and field dependence of the molar magnetic susceptibility of $Ba_3Fe_2TeO_9$ (a) as measured (b) after correction for a magnetic impurity.

the difference between them is small, ~ 5×10^{-4} cm^3 $mole^{-1}$, in the temperature range 90 < T/K < 250. They differ more obviously below ~ 90 K as they increase rapidly to a maximum at 18 K. A Curie-Weiss fit to the temperature region 250 < T/K < 300 gives θ = −167 K, and μ_{eff} = 6.74 μ_B per Fe^{3+}. The limited temperature range used limits the significance of these values and they are reported only for completeness. Fig. 5(a) also shows the ZFC susceptibility measured in 1000 Oe. There is clearly a difference between these data and those measured in 100 Oe. The field dependence of the magnetisation at 300 K, see Fig. 6(a), shows a weak remanent magnetisation, M_r ~ 5×10^{-4} μ_B per formula unit. Fig. 5(b) shows the susceptibility after subtraction of this component, that is when we assume that the sample is contaminated by a magnetically-saturated impurity (see below). The susceptibility clearly remains field-dependent at low temperature, but the effect is less marked close to room temperature. The field dependence of the molar magnetisation at 5 K is shown in Fig. 6(b); M(H) is nonlinear and a weak hysteresis is observed in low fields. The coercive field and remanent magnetisation are ~ 0.1 kOe and ~ 0.005 μ_B per formula unit, respectively.

The behaviour of χ(T), even after correction for the presence of an impurity, shows that $Ba_3Fe_2TeO_9$ does not undergo a simple transition from a paramagnetic phase to an antiferromagnetic phase at 18 K, the temperature of the susceptibility maximum. The Mössbauer spectra collected between room temperature and 13 K further illustrate the complexity of the system, see Figs. 7 and 8. No sextet indicative of the presence of a magnetically-saturated phase could be detected in the spectrum obtained over a wide velocity scale at room temperature, see Fig. 7(a). In Fig. 7(b) we show a second spectrum collected on a narrower velocity scale, also at room temperature. It is clear that at least three quadrupole-split doublets are required to fit this higher-resolution spectrum using a paramagnetic model and in Table 3 we give the fitted Mössbauer parameters for these doublets. Their isomer shifts all lie in a narrow range from 0.37 to 0.45 mm/s, indicating trivalent iron. The need to use at least three components when there are only two crystallographically-distinct iron sites might reflect the presence of occupational disorder on both of the six-coordinate sites; this will introduce many different local environments for the Fe^{3+} cations. An alternative explanation is that at 300 K the sample is close to a magnetic transition and that the peak broadening is associated with that transition. Fig. 7(c) shows the fit to a model based on two quadrupole doublets and a weakly-split sextet, the separation of the outer lines corresponding to an internal hyperfine field of only around 52 kG. We note here that this latter fit is purely *ad hoc* and serves to illustrate that we cannot rule out the presence of a weakly magnetic Fe component at room temperature. The relative subspectral areas of these three components (2 doublets and 1 sextet) at room temperature are 50(2)%, 35(3)% and 15(1)%, respectively. The relative merits of the different interpretations of these data are discussed further below. The Mössbauer spectrum observed at 200 K, see Fig. 8, is best accounted for using a doublet and a sextet. The relative area of the sextet has increased compared to that shown in Fig. 7(c) (47% cf 15%), the overall

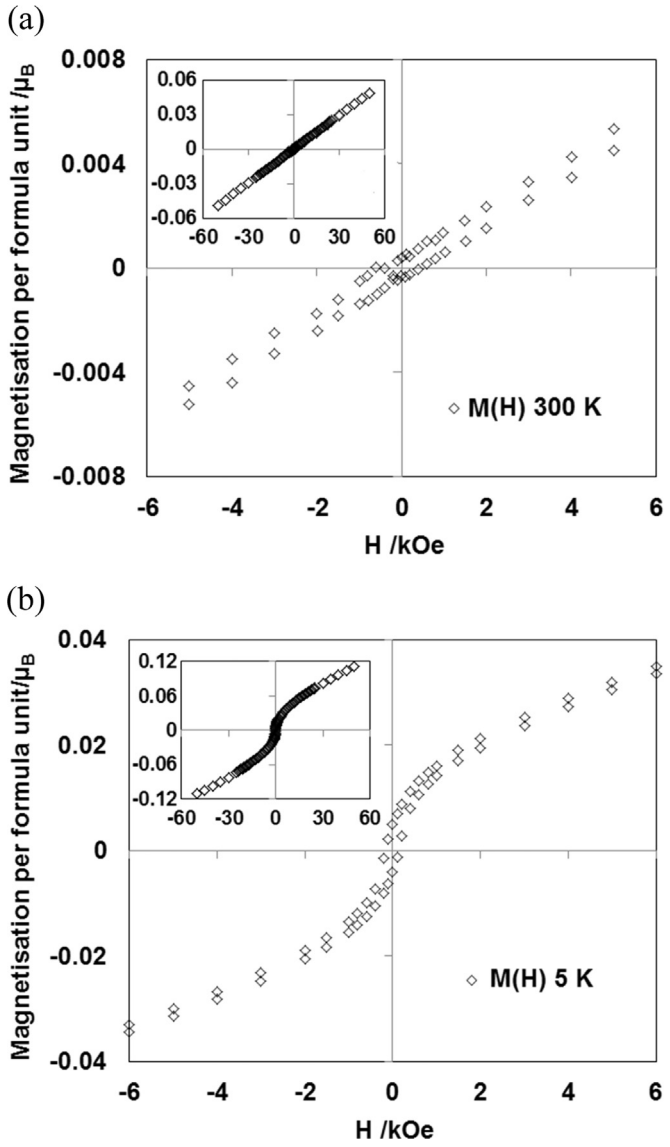

Fig. 6. Field dependence of the magnetisation of $Ba_3Fe_2TeO_9$ at (a) 300 K, (b) 5 K.

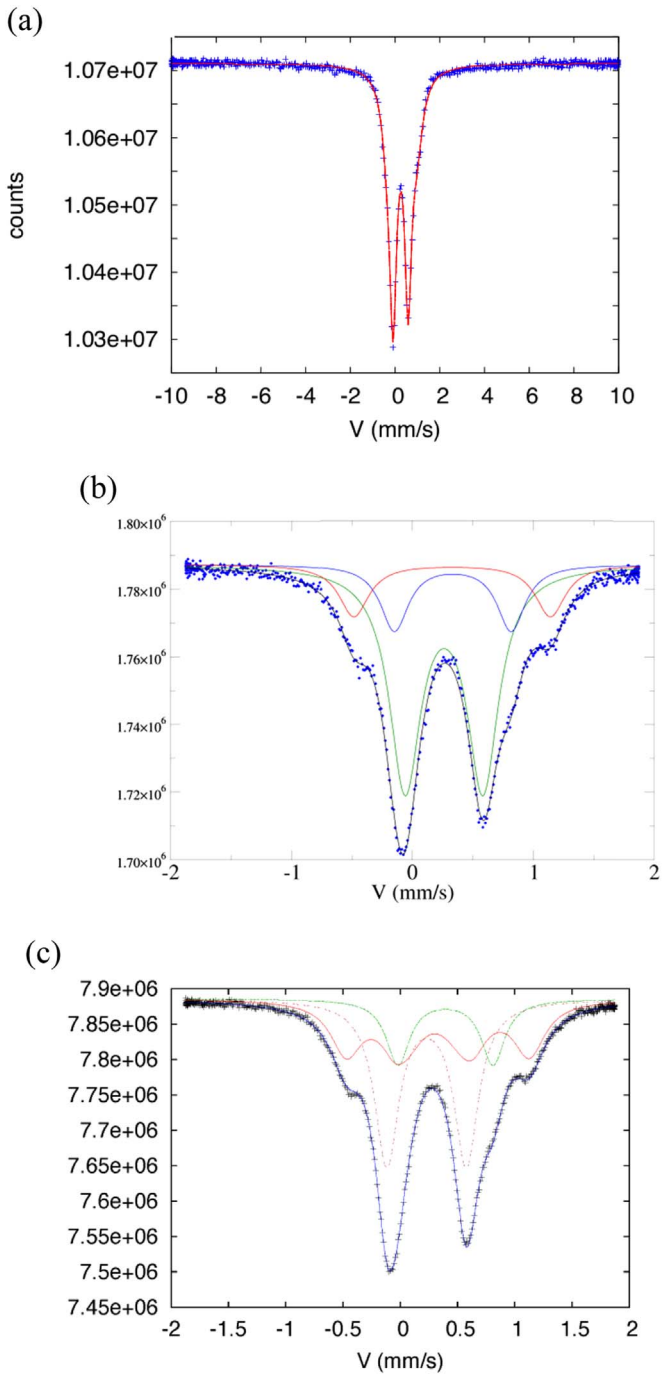

Fig. 7. ^{57}Fe Mössbauer spectra of $Ba_3Fe_2TeO_9$ acquired at room temperature (a) on an extended velocity scale; (b) on a narrower velocity scale and fitted to three doublets; (c) on a narrow velocity scale and fitted to two doublets and a sextet.

magnetic splitting has increased to H_{int} = 302 (9) kG but the individual lines are rather broad, consistent with the effects of electronic relaxation. The isomer shift and the quadrupole splitting of the lines in the doublet change little on cooling to 200 K (apart from the effect of the second-order Doppler shift on the isomer shift). After further cooling to 100 K the doublet is absent from the spectrum, which consists of six broad lines that clearly do not have a 3:2:1:1:2:3 intensity ratio. At least four overlapping sextets are needed to model the observed spectrum. The separation of the two outer maxima leads to a value of 410(2) kG for the mean hyperfine field. The 13 K spectrum shows clearly that none of the Fe^{3+} cations in $Ba_3Fe_2TeO_9$ are paramagnetic at that temperature. Furthermore, all Fe^{3+} cations experience essentially the same hyperfine magnetic field. A single-sextet fit to the 13 K spectrum yields a hyperfine magnetic field of 478(2) kG with an isomer shift of 0.514(5) mm/s, significantly larger than the weighted isomer shift of 0.398(7) mm/s measured at 295 K, reflecting the second-order Doppler shift.

The neutron diffraction data patterns collected at 3 K using wavelengths of 1.6215 Å and 2.4395 Å were analysed simultaneously using the structural model described above. Refinement of the atomic coordinates and atomic displacement did not give an entirely satisfactory account of these data. The discrepancies between the observed and calculated diffraction profiles were most noticeable at low angles and were therefore assumed to be magnetic in origin. The Bragg scattering associated with the antiferromagnetic structure illustrated in Fig. 9 accounted for the intensity mismatch, see Fig. 10. In this structure the magnetic moment of each Fe^{3+} cation is coupled in an antiparallel manner to those on the nearest-neighbour sites. The direction along which the spin vectors align could not be determined unambiguously from the neutron data alone. However, the Mössbauer spectrum collected at 13 K, see Fig. 8, allowed this issue to be resolved. Analyses of the neutron data in which the atomic moments on the 2*a* and 4*f* sites were allowed to vary independently resulted in similar values (3.40(4) and 3.40(6) μ_B per Fe^{3+} cation, respectively) at the two

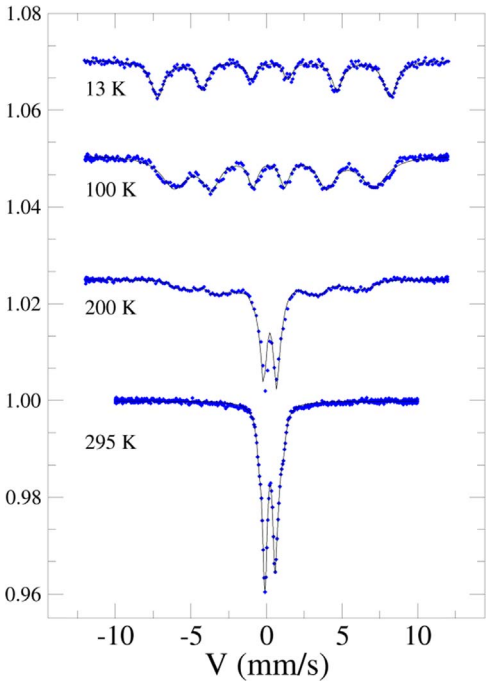

Fig. 8. ^{57}Fe Mössbauer spectra of $Ba_3Fe_2TeO_9$ acquired at 295, 200, 100 and 13 K.

Table 3
Mössbauer parameters of $Ba_3Fe_2TeO_9$, determined by fitting the higher-resolution spectrum obtained at 295 K (shown in Fig. 7b).

Spectral component	δ (mm/s)	|Δ| (mm/s)	HWHM (mm/s)	Area (%)
Doublet 1	0.375(4)	0.643(3)	0.31(2)	66.7(5)
Doublet 2	0.447(4)	0.965(7)	0.28(2)	18.0(4)
Doublet 3	0.442(4)	1.625(8)	0.30(2)	15.3(3)

δ is the isomer shift relative to α-Fe; |Δ| is the magnitude of the quadrupole splitting; HWHM is the line half-width at half maximum intensity; Area is the relative subspectral contribution to the total spectrum.

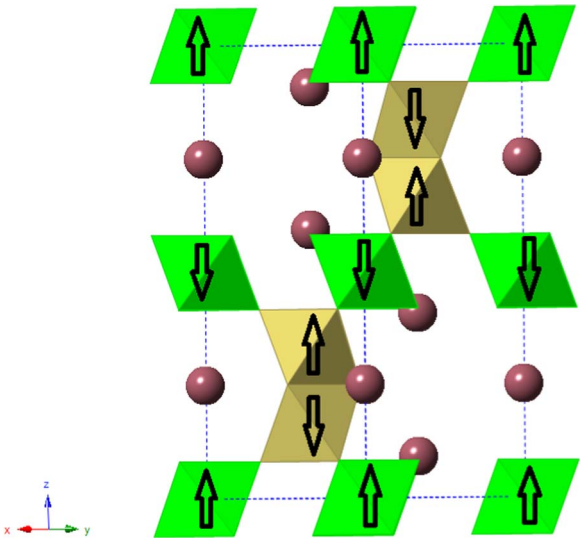

Fig. 9. Magnetic structure of $Ba_3Fe_2TeO_9$; arrows indicate the direction of ordered spins within each octahedron. Green octahedra are occupied largely by Fe and khaki octahedra are occupied by a disordered arrangement of Fe and Te. Mauve circles represent Ba atoms. (For interpretation of the references to color in this figure legend, the reader is referred to the web version of this article.)

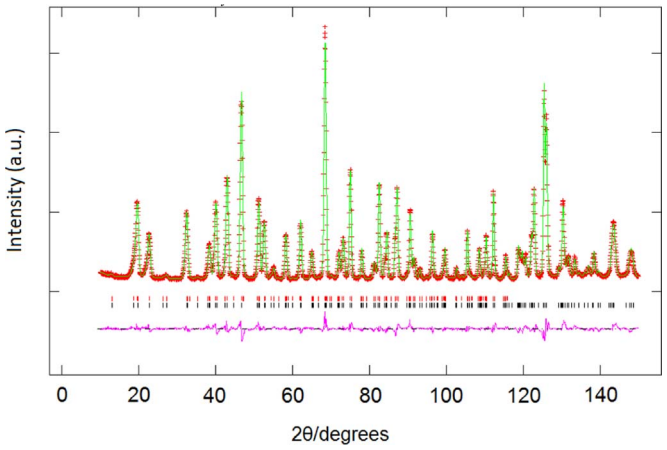

Fig. 10. Observed (red), calculated (green) neutron diffraction patterns of $Ba_3Fe_2TeO_9$ at 3 K (λ = 1.6215 Å). A difference curve (purple) is shown and reflection positions are marked. (For interpretation of the references to color in this figure legend, the reader is referred to the web version of this article.)

Table 4
Atomic parameters of $Ba_3Fe_2TeO_9$, refined from neutron diffraction data collected at 3 K.

Atom	Site	x	y	z	U_{iso}/Å^2	Fractional occupancy
Ba1	2b	0	0	0.25	0.0001(5)	1.0
Ba2	4f	⅓	⅔	0.09222(9)	0.0006(4)	1.0
Fe1	2a	0	0	0	0.0013(3)	0.933
Fe2	4f	⅓	⅔	0.85213(7)	0.0065(3)	0.529
Te1	2a	0	0	0	0.0013(3)	0.067
Te2	4f	⅓	⅔	0.85213(7)	0.0065(3)	0.471
O1	6h	0.5149(1)	0.0298(3)	0.25	0.0074(3)	1.0
O2	12k	0.8312(1)	0.6623(2)	0.08220(5)	0.0053(2)	1.0

Space group $P6_3/mmc$, a = 5.75427(4) Å, c = 14.1675(1) Å.
R_{wp} = 5.30%, R_p = 4.12%, χ^2 = 4.884.

sites only when the spins were aligned along [001], fully consistent with our Mössbauer result. Table 4 lists the refined atomic parameters and agreement factors at 3 K, and selected bond lengths are included in Table 2.

The neutron diffraction patterns collected at all temperatures 3 < T/K < 300 were analysed satisfactorily using the model described above although the magnitudes of the two moments were no longer equal; that on the sites within the dimers was greater than that on the corner-sharing sites, see Fig. 11. The values of the ordered magnetic moments, $< M_i >$, shown in Fig. 11 were derived with the assumption that all the cations take part in the long-range ordering. Our data do not allow us to distinguish between this model and one in which a fraction p_i of the cations on site i are ordered with a moment of $< M_i > /p_i$.

4. Discussion

The hexagonal crystal structure of our $Ba_3Fe_2TeO_9$ sample agrees with the structure proposed in the literature. However, the magnetic properties of our sample differ significantly from those of the samples prepared by Augsburger et al. [6] and Djerdj et al. [10]. The former appears to undergo a single ferromagnetic transition at 711 K, an unusually high transition temperature for a 6H perovskite. The most noticeable difference between our synthesis of $Ba_3Fe_2TeO_9$ and that performed by Augsburger et al. is that we used TeO_2 as the source of tellurium, while they used telluric acid as a starting material. Furthermore, Augsburger et al. used an annealing temperature of only 950 °C, lower than our choice of 1200 °C; no perovskite-like phase formed during our initial 24 h heating at 950 °C. The sol-gel protocol used recently by Djerdj et al. ended with an anneal at 1250 °C and also

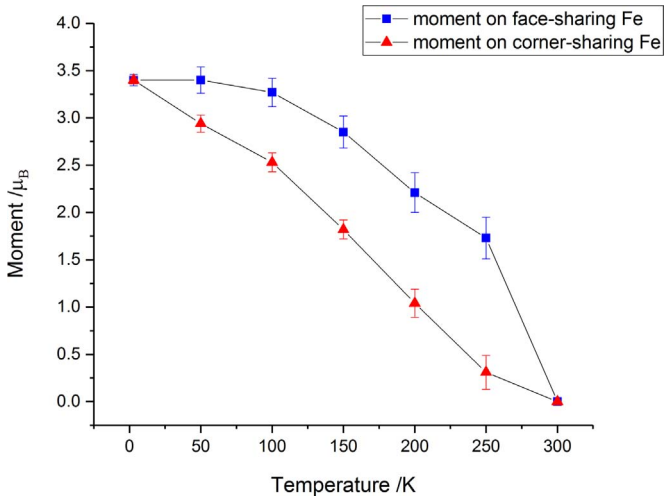

Fig. 11. Temperature dependence of the ordered magnetic moment on the 2*a* and 4*f* sites in $Ba_3Fe_2TeO_9$.

resulted in an XRD pattern characteristic of a 6H perovskite. However, the magnetic behaviour of their sample also differs from that of our own. They observed the transition at ~ 20 K reported above but the ZFC and FC susceptibilities they measured in 100 G are markedly different below ~ 80 K. They did not detect the transition at 711 K reported by Augsburger et al. but the susceptibility of their sample was nevertheless field-dependent at room temperature. It is clear that variations in the synthesis method can have significant consequences for the properties of the final product. In the following paragraphs we present what we believe is a self-consistent account of the behaviour of our sample.

We shall discuss the data collected at room temperature and below the temperature of the susceptibility maximum and then consider the more complex behaviour observed at intermediate temperatures. The shift from a pseudo-cubic perovskite in the case of $Sr_3Fe_2TeO_9$ to a 6H structure in the case of $Ba_3Fe_2TeO_9$ reflects the well-established dependence of the structure type on the radius ratio r_A/r_B. $Ba_3Fe_2WO_9$ is also a 6H perovskite [16], whereas $Ba_3Bi_2TeO_9$ [17] has the same trigonal structure as our $Sr_3Fe_2TeO_9$ sample and $Sr_3Fe_2WO_9$ is a tetragonal, pseudo-cubic perovskite [18]. Despite the discrepancies in the magnetic properties discussed above, the structural parameters derived from our room-temperature neutron diffraction study are, with the exception of the Fe:Te distribution over the 2*a* and 4*f* sites, in excellent agreement with those determined by Augsburger et al. Table 1 shows an Fe:Te ratio of 0.933: 0.067 on the 2*a* site, significantly larger than that reported in the earlier work. The mean bond length around the 4*f* site, 1.994 Å, is shorter than that around the 2*a* site, consistent with a lower concentration of the larger Fe^{3+} cations on the former site. At room temperature there is no evidence of magnetic Bragg scattering in the neutron data.

All the bond lengths listed in Table 2 are shorter at 3 K than at 300 K, as is to be expected. There is, however, no significant structural change on cooling. The additional Bragg scattering present in the neutron diffraction data collected at 3 K identified the presence of long-range magnetic ordering, and the antiferromagnetic structure shown in Fig. 9 is consistent with the observed intensity distribution. The magnitude of the mean ordered moment determined by neutron diffraction, 3.40 μ_B per cation, is lower than that determined in many antiferromagnetic compounds of Fe^{3+} [19–22], suggesting that not all the Fe^{3+} cations take part in the long-range magnetic ordering. The absence of a central resonance in the Mössbauer spectrum recorded at 13 K suggests that any decoupled spins freeze in a glassy state rather than remaining paramagnetic. The presence of only one sextet in this spectrum, albeit with some evidence of peak broadening, shows that the glassy spins experience essentially the same internal hyperfine field as those that are coupled to the magnetically-ordered backbone. The magnitude of the field is somewhat low for a compound of Fe^{3+}, but not anomalously so. This model is consistent with our magnetometry data, wherein the field dependence of χ(T) and the hysteresis observed below the temperature of the susceptibility maximum, see Fig. 5, are both characteristic not of generic antiferromagnetic behaviour but rather of spin glasses. The cations that are decoupled from the magnetic ordering are likely to be those in octahedra that are linked to a disproportionately high fraction of TeO_6 octahedra, and thus are part of relatively few Fe–O–Fe superexchange pathways. The magnetic ordering shown in Fig. 9 propagates through the three-dimensional structure without frustration despite the fact that 33% of the octahedra are occupied by diamagnetic cations.

The NPD data and Mössbauer spectra collected between room temperature and 13 K reveal additional complexity in the electronic properties of $Ba_3Fe_2TeO_9$. The diffraction data reveal that the two crystallographic sites containing Fe^{3+} are both involved in long-range magnetic ordering in this temperature range. However, the magnetisations of the sublattices saturate at different rates. As explained above, the correlation between the fraction of ordered spins and their moment prevents an unambiguous determination of the ordered fraction from the neutron data. The Mössbauer spectrum observed at 200 K shows that at this temperature around 47(5)% of the Fe^{3+} spins are static on a timescale of 10^{-7} s while the remainder relax more rapidly. Any spin that is static on the Mössbauer timescale will be static on the shorter timescale associated with magnetic neutron diffraction. However, we cannot know whether they are involved in long-range magnetic ordering or whether they are in a glass-like state. Those in the former group are responsible for the magnetic Bragg scattering observed in the NPD patterns. At 100 K all the spins are static on the Mössbauer timescale but a wide range of internal hyperfine fields appears to be present. Again it seems likely that some of these static spins are part of the magnetically-ordered network detected by neutron diffraction whereas the remainder are in regions showing only short-range magnetic order. We expect the latter to occur where there is a relative excess of Te^{6+}, for example in the vicinity of Te_2O_9 dimers, and the former in regions where –Fe–O–Fe–O– superexchange interactions can most readily percolate through the structure, for example in the vicinity of Fe_2O_9 dimers.

It is clear from these data that the onset of magnetic ordering in $Ba_3Fe_2TeO_9$ occurs at a temperature higher than that suggested by both our susceptibility data and those collected by Djerdj et al.; neither the susceptibility maximum at 18 K nor the change in gradient of χ^{-1}(T) at ~ 90 K correspond to the ordering temperature. It seems likely that the hysteresis observed below 90 K indicates the presence of blocked spin-clusters [23–25] and that the spins that do not participate in the long-range ordering form a spin-glass below 18 K. There are no features at higher temperatures in χ(T) that indicate an alternative transition temperature. We tentatively propose that it lies very close to 300 K. This is consistent with the interpretation of the Mössbauer spectrum acquired at room temperature in terms of a quadrupole doublet from each of the distinct octahedral sites and a developing sextet, rather than in terms of three doublets of uncertain parentage.

The above account of $Ba_3Fe_2TeO_9$ bears some similarity to that of $Ba_3Fe_2WO_9$ given previously [16], although there are also differences. The 2*a* sites in that 6H perovskite were found to be occupied only by Fe^{3+}; the cation disorder seen in $Ba_3Fe_2TeO_9$ is absent in the tungsten analogue. The available neutron diffraction patterns showed that $Ba_3Fe_2WO_9$ is paramagnetic at room temperature and antiferromagnetic at 200 K although the temperature gradient of the sample magnetisation was constant and negative for 100 < T/K < 400, implying that not all the spins participate in the long-range ordering. Furthermore, the magnetic moments at the Fe1 and Fe2/W2 sites were found to be low and different, 3.24 and 3.93 μ_B respectively, throughout the temperature range 10 < T/K < 200. The neutron data on $Ba_3Fe_2WO_9$ are consistent with an earlier Mössbauer study that

reported a Néel temperature of 223 K [9], close to the temperature at which the hysteresis in the susceptibility of $Ba_3Fe_2TeO_9$ becomes clear.

In order to account for the field-dependence of χ(T) at temperatures close to 300 K we have assumed that our sample contains a magnetic impurity, the concentration of which is too low to be detected by XRPD, NPD or Mössbauer spectroscopy. $BaFe_{12}O_{19}$ has a Curie temperature of 723 K and a saturation magnetisation of ~ 40 emu g^{-1} [26,27]. An impurity level of 1 part in 10^4, undetectable using the above techniques, would therefore be enough to account for the room-temperature magnetisation of our sample. We note that the Curie temperature of the ferrite is close to the ferromagnetic transition temperature reported by Augsburger et al. for $Ba_3Fe_2TeO_9$.

5. Conclusions

$Ba_3Fe_2TeO_9$ is a 6H perovskite in which the cation sites in the face-sharing octahedra are occupied randomly by Fe^{3+} and Te^{6+} in a ratio that is close to, but different from, 1:1. The sites in the vertex-sharing octahedra are occupied predominantly by Fe^{3+} although some Te^{6+} is also present. At a temperature close to 300 K the atomic moments begin to order in an antiferromagnetic manner. A backbone of ordered spins forms within the structure and on further cooling more spins join the backbone. Spins in locally iron-rich regions order before those in regions where the superexchange pathways are prevented from percolating by a local excess of Te^{6+}. The spins that are unable to take part in the long-range magnetic order form clusters that freeze to form a spin glass at 18 K.

Acknowledgments

We thank EPSRC for financial support through grant EP/M018954/1.

References

[1] E.J. Cussen, P.D. Battle, Chem. Mater. 12 (2000) 831.
[2] H. Krischner, K. Torkar, B.O. Kolbesen, J. Solid State Chem. 3 (1971) 349.
[3] P.D. Battle, T.C. Gibb, A.J. Herod, S.-H. Kim, P.H. Munns, J. Mater. Chem. 5 (1995) 865.
[4] P.C. Donohue, L. Katz, R. Ward, Inorg. Chem. 5 (1966) 335.
[5] S.A. Ivanov, P. Nordblad, S.G. Eriksson, R. Tellgren, H. Rundlof, Mater. Res. Bull. 42 (2007) 776–789.
[6] M.S. Augsburger, M.C. Viola, J.C. Pedregosa, R.E. Carbonio, J.A. Alonso, J. Mater. Chem. 16 (2006) 4235–4242.
[7] Y. Tang, E.C. Hunter, P.D. Battle, R. Paria Sena, J. Hadermann, M. Avdeev, J.M. Cadogan, J. Solid State Chem. 242 (2016) 86–95.
[8] D. Harari, J.C. Bernier, P. Poix, J. Solid State Chem. 5 (1972) 382–390.
[9] V.V. Gagulin, N.V. Fadeeva, A.G. Belous, A.V. Titov, K.P. Mitrofanov, M.V. Plotnikova, S.P. Soloviev, Y.N. Venevtsev, Phys. Status Solidi a-Appl. Res. 48 (1978) 183–189.
[10] I. Djerdj, J. Popović, S. Mal, T. Weller, M. Nuskol, Z. Jagličić, Ž. Skoko, D. Pajić, C. Suchomski, P. Voepel, R. Marschall, B. Kozlevčar, B.M. Smarsly, Cryst. Growth Des. 16 (2016) 2535–2541.
[11] A.C. Larson, R.B. von Dreele, General Structural Analysis System (GSAS), Los Alamos National Laboratories, Laur, 1990, pp. 86–748.
[12] H.M. Rietveld, J. Appl. Crystallogr. 2 (1969) 65–71.
[13] B. van Laar, W.B. Yelon, J. Appl. Crystallogr. 17 (1984) 47–54.
[14] C. Koch, Determination of Core Structure Periodicity and Point Defect Density along Dislocations (Ph.D. thesis), Arizona State University, 2002.
[15] R.A. Brand, ⟨http://www.wissel-instruments.de/⟩.
[16] S.A. Ivanov, S.G. Eriksson, J. Erikssen, R. Tellgren, H. Rundlof, Mater. Res. Bull. 39 (2004) 615–628.
[17] J.H. Park, P.M. Woodward, Int. J. Inorg. Mater. 2 (2000) 153–166.
[18] S.A. Ivanov, S.G. Eriksson, R. Tellgren, H. Rundlof, Mater. Res. Bull. 36 (2001) 2585–2596.
[19] P.D. Battle, G.R. Blake, T.C. Gibb, J.F. Vente, J. Solid State Chem. 145 (1999) 541–548.
[20] G.J. Long, G. Longworth, P. Battle, A.K. Cheetham, R.V. Thundathil, D. Beveridge, Inorg. Chem. 18 (1979) 624–632.
[21] P.D. Battle, T.C. Gibb, P. Lightfoot, J. Solid State Chem. 84 (1990) 237.
[22] W.C. Koehler, E.O. Wollan, J. Phys. Chem. Solids 2 (1957) 100.
[23] D. Fiorani, S. Viticoli, J.L. Dormann, J.L. Tholence, A.P. Murani, Phys. Rev. B 30 (1984) 2776.
[24] S.H. Kim, P.D. Battle, J. Magn. Magn. Mater. 123 (1993) 273.
[25] A. Labarta, R. Rodriguez, L. Balcells, J. Tejada, X. Obradors, F.J. Berry, Phys. Rev. B 44 (1991) 691.
[26] K. Haneda, H. Kojima, J. Appl. Phys. 44 (1973) 3760–3762.
[27] J.J. Went, G.W. Rathenau, E.W. Gorter, G.W. Vanoosterhout, Phys. Rev. 86 (1952) 424–425.